Journal of Inorganic and Organometallic Polymers and Materials
https://doi.org/10.1007/s10904-025-03710-x

RESEARCH

DFT-Based Investigation of Opto-Electronic, Mechanical, and Thermoelectric Properties of Sr_2YBiO_6 for Green Energy Applications

Aparna Dixit[1] · Arti Saxena[1,2] · Mumtaz Manzoor[3] · Sadaf Sahid[4] · Ramesh Sharma[5] · Ahmed Ahmed Ibrahim[6] · Mohammad A. El-Meligy[7,8] · Barno Abdullaeva[9] · Vipul Srivastava[10]

Received: 21 December 2024 / Accepted: 3 March 2025

Abstract
The present study on double perovskite Sr_2YBiO_6 has used a full potential linearized augmented plane wave (FP-LAPW) approach in conjunction with density functional theory (DFT) and semiclassical Boltzmann theory. The study has used PBE-GGA, PBE-sol, mBJ, mBJ + SOC exchange potentials to obtain clear electronic structure of the material. The electronic structure analysis indicates that Sr_2YBiO_6 compound exhibits semiconductor behavior with an indirect energy gap of 2.150 eV, using TB-mBJ. Further, material is mechanically and thermodynamically stable. The no negative frequencies in the phonon spectra confirm dynamical stability as well. This study investigates optical properties of Sr_2YBiO_6, including dielectric function, refractive index, electrical conductivity, absorption, reflectivity and electron loss function. We report static optical reflectivity 0.085, which expresses, 8.5% of incident light is reflected rest is absorbed. A static refractive index is estimated to be 1.82, suggests that Sr_2YBiO_6 has moderate optical density and transparency in the long-wavelength range, which is useful in designing optical and photonic devices. Further, on the ground of thermoelectric performances, the values for Seebeck coefficient, power factor and figure of merit are estimated to be 214.8 μV/K, 7.34 10^{11}W/K^{2}ms and 0.062 at 300 K, respectively. The value of figure of merit increases to 0.7 at high temperature of 1200 K. Thermodynamic behavior and elastic properties have also been investigated for this compound. Our computed results are in accordance with the other double perovskites. The findings demonstrate that this double perovskite material is outstanding for both UV and visible-light photovoltaic applications, as well as for thermoelectric devices.

Keywords Double Perovskites · Thermoelectric · First Principles · Electronic Band Structures

✉ Mumtaz Manzoor
mumtazmanzoor95@gmail.com

✉ Ramesh Sharma
sharmadft@gmail.com

✉ Vipul Srivastava
vipsri27@gmail.com

[1] Department of Basic Sciences and Humanities, Pranveer Singh Institute of Technology, Kanpur, U.P, India

[2] Department of Electronics & Communication, Pranveer Singh Institute of Technology, Kanpur, India

[3] Institute of Physics, Slovak Academy of Sciences, 845 07 Bratislava, Slovakia

[4] Department of Physics, Riphah International University, Lahore, Pakistan

[5] Department of Applied Science, Feroze Gandhi Institute of Engineering and Technology, Raebareli, U.P 229001, India

[6] Department of Physis & Astronomy, College of Science, King Saud University, P.O. Box 2455, Riyadh 11451, Saudi Arabia

[7] Jadara University Research Centre, Jadara University, P.O.Box 733, Irbid, Jordan

[8] Applied Science Research Center, Applied Science Private University, Amman, Jordan

[9] Department of Mathematics and Information Technologies, vice-Rector for Scientific Affairs, Tashkent State Pedagogical University, Tashkent, Uzbekistan

[10] Department of Physics, School of Chemical Engineering and Physical Sciences, Lovely Professional University, Phagwara, Punjab 144411, India

Published online: 10 March 2025

1 Introduction

In recent years, perovskites have become a focal point of research due to their wide range of applications. These compounds are crucial in ground breaking fields like spintronics technology [1], solar cells [2], and solid oxide-based fuel cells [3]. Double-perovskite (DP) oxides are known for their exceptional physical properties, leading to their diverse use in areas such as thermoelectric materials [4], heterogeneous catalysis [5], photovoltaic cells, and photocatalysis [6]. Their impressive attributes make them particularly valuable for various industrial applications [7]. As industrialization advances and the demand for natural resources grows, there is an increasing imperative to lessen energy ingesting and pursue substitute sources [8]. To contend expanding ecological contamination and energy dearth, there is a need for the development of environmentally friendly and sustainable energy sources [9]. The thermoelectric figure of merit (ZT) is used to evaluate the performance of thermoelectric materials [10] and is calculated based on four key factors: $ZT = \frac{S^2 \sigma T}{(\kappa_e + \kappa_l)}$ where T is absolute temperature, S is Seebeck coefficient, σ is electrical conductivity, κ_l is lattice thermal conductivity, and κ_e is electronic thermal conductivity [11]. These factors collectively determine the effectiveness of a thermoelectric material. Thermoelectric materials, which can transform waste heat into electrical energy, have gained significant global interest as eco-friendly energy sources [12]. The present requirement to lessen the dependence on traditional fossil fuels underscores the importance of these materials [13]. Perovskite materials are especially notable for their impressive thermoelectric properties and are extensively used in thermoelectric devices [14]. Recently, there has been increasing focus on their application in high-temperature thermoelectric research [15, 16]. Recent applications of DFT have focused on exploring the optical, thermoelectric, and electronic properties of not only double perovskite (DP) oxides [17–24] but various materials [25–43].

Rameshe et al. studied the various properties of $Sr_2Al(Nb/Ta)O_6$ in cubic phase and found that Sr_2AlNbO_6 and Sr_2AlTaO_6 were semiconductors with a direct band gap [44]. They also calculated the optical properties, including the real and imaginary parts of the dielectric function, for both materials. Meanwhile, Haid et al. examined Sr_2CrTaO_6, investigated its ground state properties and its half-metallic ferromagnetic behavior [45]. Parrey et al. [46] investigated the spin-oriented bands of La_2NbMnO_6 and confirmed its half-metallicity. Due to its substantial absorption across ultraviolet and infrared frequencies, this material is well-suited for use in optoelectronic devices designed for these spectral ranges. Dar et al. [47] provided insights into the thermoelectric behaviour of Ba_2InTaO_6, demonstrating that the material functioned as a semiconductor with electrons as the majority charge carriers. Their results also highlighted that Ba_2InTaO_6 exhibited a high-power factor, suggesting its potential for use in thermoelectric devices. Khandy et al. [48] studied Ba_2CdReO_6 and confirmed its stability in ferromagnetic state. Their analysis of the band structure indicates that the material exhibits half-metallic behavior. These properties make it a promising candidate for applications in spintronics, spotlight technologies, and as an electrode material. Al-Qaisi et al. [49] studied the optoelectronic characteristics of Ba_2NaIO_6 and found that it functioned as a p-type semiconductor with a direct band gap. Aziz et al. [50] examined the properties of X_2NaIO_6 with X = Pb or Sr and found that the investigated materials belong to semiconductor-family. Pb_2NaIO_6 unveiled a direct band gap of 3.75 eV, while Sr_2NaIO_6 a band gap of 5.48 eV. Additionally, Sr_2NaIO_6 achieved a higher ZT value of 0.773 compared to Pb_2NaIO_6. The cubic phases of these materials are considered suitable for thermoelectric and optoelectronic device applications. Hanif et al. [51] conducted a theoretical investigation of the semiconducting compounds Sr_2XNbO_6 (where X = La or Lu). Their results suggest that the examined materials are promising contenders for applications in the Ultraviolet (UV) region. Alongside experimental investigations of oxide and halogen-based double perovskite compounds for their thermoelectric properties, numerous theoretical studies have utilized first-principles for investigating band structure and Boltzmann transport theory to analyze these materials. Pillai et al. [52]. have synthesized Ba_2YBiO_6 nanoparticles using low temperature sol-gel technique. The examination of XRD data reveals that the synthesized compound exhibits cubic perovskite ($A_2BB'O_6$-type) phase. On the other hand, some other experimental techniques such as Tunneling electron microscope (TEM) and Scanning electron microscope (SEM) micrograph confirmed the behavior of powder (20–40 nm) nature and found that size of grain varies between 0.07 and 0.21 μm respectively. The energy gap of Ba_2YBiO_6 has been found to be 2.78 eV as scrutinized by UV–vis spectrometry. However, Sr_2YBiO_6, a prominent member of the perovskite's family, has not been investigated for its structural, optoelectronic as well as thermoelectric characteristics. As a result, the current literature does not provide an efficient study of this compound. Therefore, (i) lack of studies on Seebeck coefficient, electrical conductivity, and thermal conductivity based on Boltzmann Transport Theory for thermoelectric applications (ii) insufficient analysis on the role of hybridization between Bi-6s, Y-4d, and O-2p orbitals, influencing band structure and electronic performance (iii) no theoretical insights into absorption coefficient, refractive index, and dielectric function, which are vital for photonic and photovoltaic applications

have motivated us to perform this study. The present venture inspects the structural, electronic, elastic, and transport properties of DP Sr_2YBiO_6 with a cubic structure using the most effective DFT approach. Recently, Pan et al., predicted the improved electronic and optical properties of semiconductors by first principles methods [67–70]. The material Sr_2YBiO_6 is chosen for the reason of (i) lead-free and environmentally friendly nature (ii) the presence of Bi^{3+} and Y^{3+} in a double perovskite structure influences bandgap tenability (iii) expected to exhibit high Seebeck coefficient and optical absorption, making it promising for renewable energy technologies.

We utilize ab initio method along with the Boltzmann transport theory, applying stiff band as well as persistent relaxation time estimates for charge carriers. The relaxation time (τ) in the present calculations is considered by constant relaxation time approximation (CRTA), where τ is treated as a fitting parameter. Its constant value in the present calculations is taken as 1×10^{-14} sec. Our findings show that Sr_2YBiO_6 is a semiconductor with narrow band gaps, making them potential candidates for thermoelectric applications. We also evaluate the mechanical stability by calculating elastic constants C_{ij}. Additionally, we analyze the thermoelectric properties over a range of chemical potentials ranging between −2.0 eV and 4.0 eV at 300 K, 700 K, and 1200 K. There is currently a shortage of theoretical and experimental evidence on these materials' elastic and thermoelectric properties. The article is organized into sections: "Computational Methods" describes the techniques used, "Results and Discussion" presents the findings, and "Conclusion" summarizes the overall results.

2 Computational Method

In the present investigation, we executed DFT-based calculations utilizing the full potential linearized augmented plane wave (FP-LAPW) method [53]. The calculations were performed using the WIEN2k code [54], which is well-matched for determining the electronic behavior of solids. The structural parameters of Sr_2YBiO_6 were calculated using the PBE-GGA [55] as well as LDA method to evaluate the inclusion of the exchange-correlation potential approximation. Although PBE-GGA accurately determines structural properties ground state energies, it typically underestimates the band gap in semiconductors. To address this issue, modified potential like modified Becke-Johnson (mBJ) [56] potential has been used for the computation of band gap accurately. The mBJ exchange potential, implemented via the Trans-Blaha (TB) method, was found to be the most suitable for accurately predicting the electronic structure of the material. However, we have computed electronic structure using LDA, PBE-GGA, PBE-sol and mBJ+SOC potentials. LDA and PBE-GGA tend to underestimate band gaps significantly due to their inherent self-interaction errors. PBE-sol (PBE for solids) is slightly better than PBE-GGA for lattice parameters but does not improve band gap predictions. mBJ+SOC improves band gaps but is necessary only for materials with strong relativistic effects. TB-mBJ corrects the band gap underestimation effectively, often providing values close to experimental results without requiring expensive hybrid functionals [57–61].In the DFT procedure, the unit cell was apportioned into interstitial regions and non-overlapping of muffin-tin spheres. In the interstitial region, wave functions were expanded as a linear combination of radial functions and spherical harmonics, with l values extending up to 10. The charge density was expanded using a Fourier series and curtailed at $G_{max} = 12\, a.u.$ For the single-electron wave functions, the cutoff parameter $R_{MT} * K_{max}$ was set to 7 to increase the plane-wave basis set in the constant potential region. In this context, R_{MT} represents the atomic radii of muffin tin spheres, and in reciprocal space, K_{max} is the biggest K-vector applied to the smallest unit cell. The muffin-tin radii (R_{MT}) used were 1.73 a.u. for Sr, 2.12 a.u. for Y, 2.12 a.u. for Bi, and 2.5 a.u. for O. Self-consistent calculations, where the electron density, potential, and energy are mutually consistent, are used to solve KS Eqs. [62, 63]. Iterating up to 0.0001e for charge convergence between subsequent cycles and iterating up to 0.0001Ry improves energy convergence. All the investigated properties were determined using Monkhorst Pack grid of $14 \times 14 \times 14$ k-points for the studied compound. A finer k-point mesh of $36 \times 36 \times 36$ was employed for accurate determination of the final electronic structures. The optical properties were calculated using a dipole-matrix approach in the WIEN2k package, with a broadening parameter of 0.1 eV applied to the spectra [64]. To assess the thermoelectric performance as a variable of temperature and chemical potential in the BoltzTraP code, which rely on rigid band approximation, was used. The transport distribution is integrated to provide the electrical conductivity (σ) and Seebeck coefficient (S) as functions of chemical potential ($\mu - \epsilon_F$) and absolute temperature (T).

3 Results and Discussion

3.1 Structural Properties

To analyze the structural properties of Sr_2YBiO_6, we utilized the Birch's equation of state in relation to the unit cell volume and optimized with PBE-GGA and LDA using the experimental lattice parameters [17], as illustrated in Figs.

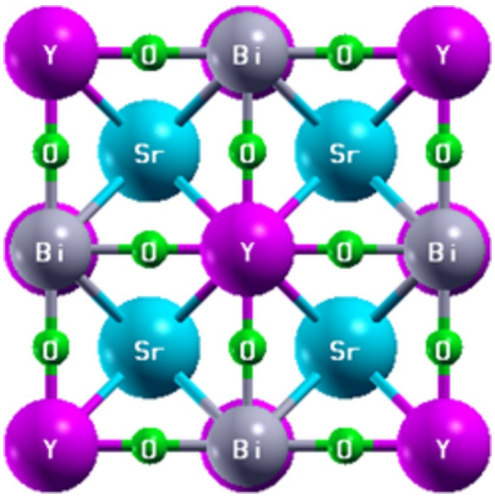

Fig. 1 Optimized crystal structure of double perovskite Sr_2YBiO_6 in the space group cubic Fm-3 m. The figure is produced using X-Crysden software, which is embedded in WIEN2k code

1 and 2. The experimental lattice parameter of Sr_2YBiO_6 was measured as 8.627 Å in its cubic phase, which crystallizes in the Fm-3 m space group. In the unit cell, the Wyckoff positions are as follows: Sr atoms are at (1/4, 1/4, 1/4), Bi atoms are at (0, 0, 0), Y atoms are at (0, 0, 0.5), and O atoms are at (0, 0, 0.2439). The equilibrium state structural parameters, including lattice constants (a_0), bulk modulus (B) and its pressure derivative (B′), and, using PBE-GGA and LDA are detailed in Table 1. The calculated results of lattice constant with PBE-GGA show well agreement with the available experimental results which confirm the accuracy of the present calculations. The melting temperature of the investigated DP is calculated to be 1898.738 K.

The cohesive energy as well as formation energy of the studied compound are also studied to confirm its stability and presented in Table 1.

$$E_f = \frac{E_{Sr2YBiO6} - (2E_{Sr} + E_Y + E_{Bi} + 6E_O)}{10} \quad (1)$$

The negative value of E_f indicates their stability as well as the amount of energy gets released during the formation of the studied DP. In addition to this, cohesive energy of the compound is also computed using the relation:

$$E_C = \frac{(2E_{Sr} + E_Y + E_{Bi} + 6E_O) - E_{Sr2YBiO6}}{10} \quad (2)$$

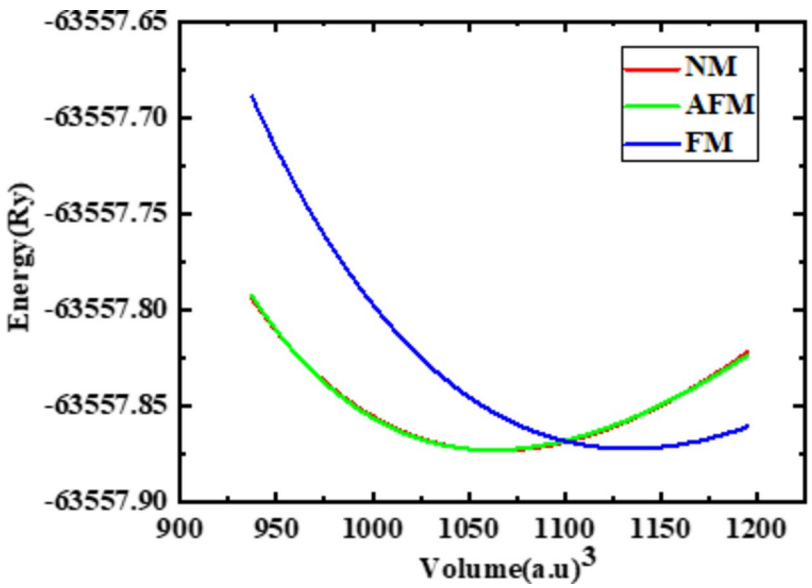

Fig. 2 The Energy versus volume optimization graph of Sr_2YBiO_6, where NM (red color) represents non-magnetic phase, AFM (green color) represents anti ferromagnetic phase and FM (blue) represents ferro-magnetic phase (Color figure online)

Table 1 Calculated lattice parameter *a* (Å), bulk modulus *B*, its derivative B_P, the minimum total energy E_{tot}, energy of cohesion E_{coh}, enthalpy of formation E_f, tolerance factor (t_f), bader charges (Å) and effective mass of double perovskite Sr_2YBiO_6

XC	a (Å)	V ($a.u^3$)	B (GPa)	B.*P*	E_{tot}(Ry)	E_c (eV/atom)	E_f (eV/atom)	Bader charges (Å)	t_f	Effective mass
FM-GGA	8.57	1064.60	118.14	4.51	− 63557.872	5.069	− 2.594	Sr=1.58	0.894	$m_e^* = 2.10$
AFM-GGA	8.57	1062.40	116.34	6.41	− 63557.873			Y=1.86		$m_h^* = 1.08$
NM-GGA	8.57	1064.53	117.71	4.98	− 63557.873			Bi=2.37		
Ref.	8.34[a]	978.56[a]	150.48[a]	4.65[a]	− 69235.930[a]	5.53[a]	− 2.853[a]	O=−1.23	0.99[b]	
	8.13[b]		124.05[b]	4.86[b]	− 29911.696[b]	4.58[b]				

[a]Ref. [15], [b]Ref. [18]

where $E_{Sr2YBiO6}$ denotes the total energy of the compound and E_{Sr}, E_Y, E_{Bi}, E_O their individual energies. The positive value of 5.069 eV/atom again reveals that the studied DP is stable in cubic phase. From the values of formation energy as well as cohesive energy, the mechanical stability of the compound has been confirmed. The tolerance factor (t_G) for perovskites is computed using equation is

$$t_G = \frac{R_{Sr} + R_O}{\sqrt{2}\left(\frac{R_Y + R_{Bi}}{2} + R_O\right)} \tag{3}$$

where, $R_{Sr/Y/Bi/O}$ are effective ionic radii of individual elements obtained from the Shannon ionic radius. The computed tolerance factor has been computed and tabulated in Table 1. If t_G lies between 0.80 and 1.0, the perovskite is said to be stable in cubic phase. As observed from Table 1, t_G is obtained to be 0.894, showing that the studied DP Sr_2YBiO_6 is stable in its cubic phase. Our results are compared with the available similar DPs [15, 18], a good agreement is presented.

To evaluate the dynamical stability of Sr_2YBiO_6 perovskites, phonon dispersion calculations were performed using the Vienna Ab-initio Simulation Package (VASP) [65]. The dynamical stability of a material is directly linked to its phonon dispersion, which depicts the dependence of phonon frequencies on wavevectors throughout the Brillouin zone. The results are displayed in the phonon dispersion curve (PDC) in Fig. 3. The absence of any negative (imaginary) frequencies across the Brillouin zone confirms that the examined double perovskites are dynamically stable [66].

3.2 Electronic Properties

For the brief analysis of electronic properties, we have energy band structure with total and partial density of states (Figs. 4 and 5) that aids in distinguishing the material behaviour to gain understanding of the field or area in which their possible technological applications may be used. Usually, it is seen that PBE-GGA computations underrates the band gap in semiconductors and insulators. The primary reason for this is that its basic structure is too rigid to accurately capture the exchange-correlation potential and its charge derivative. The TB-mBJ approximation employed in the present paper has been effectively utilized in various recent papers as a substitute for the underestimating of the band-gap [17–24].

Figure 4(a–d) illustrated the computed electronic band plot in k-space along high-symmetry paths $W - L - \Gamma - X - W$ using different approximations like LDA, PBE-GGA, mBJ and mBJ+Spin orbital coupling (SOC). The electronic band structures calculated using all four different exchange potential are found to be similar in nature and the value of obtained band gaps are listed in Table 2. From Fig. 3, it can be seen that with PBE-GGA and mBJ, Sr_2YBiO_6 is an indirect band-gap semiconductor with the value of 2.150 eV (displayed in Table 2), between the top most the valence band at Γ-point and the bottom most in the conduction band at X-point, respectively. This calculated energy band gap (E_g) agreed well with the pervious reported theoretical data of similar compounds, in the literature [19–24, 67, 68]. The examined DP's indirect energy gaps, which cause phonon excitations when electrons move from the bottom of the conduction band to the direct band, balance the wave vector. As a result, it limits the devices' time performance and makes them better suited to thermoelectric qualities.

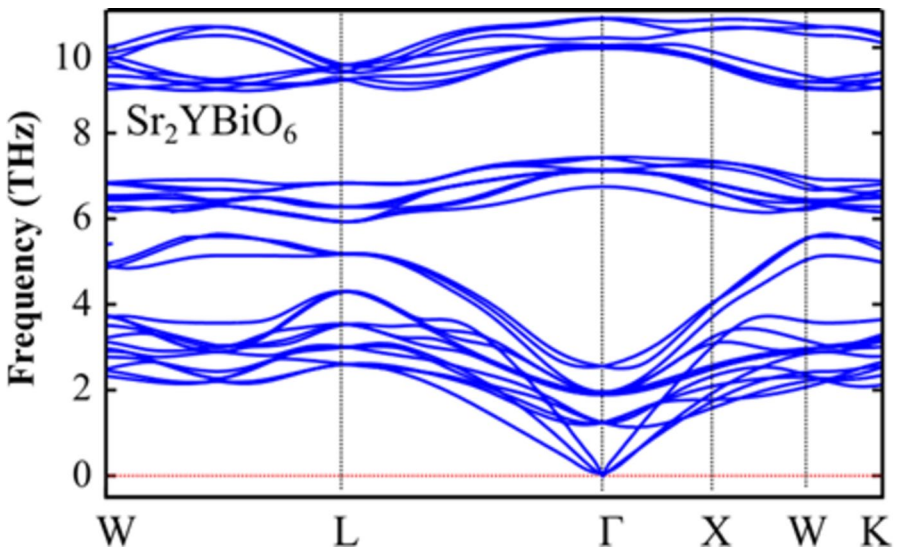

Fig. 3 Computed phonon dispersion curve for double perovskite Sr_2YBiO_6. No negative frequencies confirm its dynamical stability

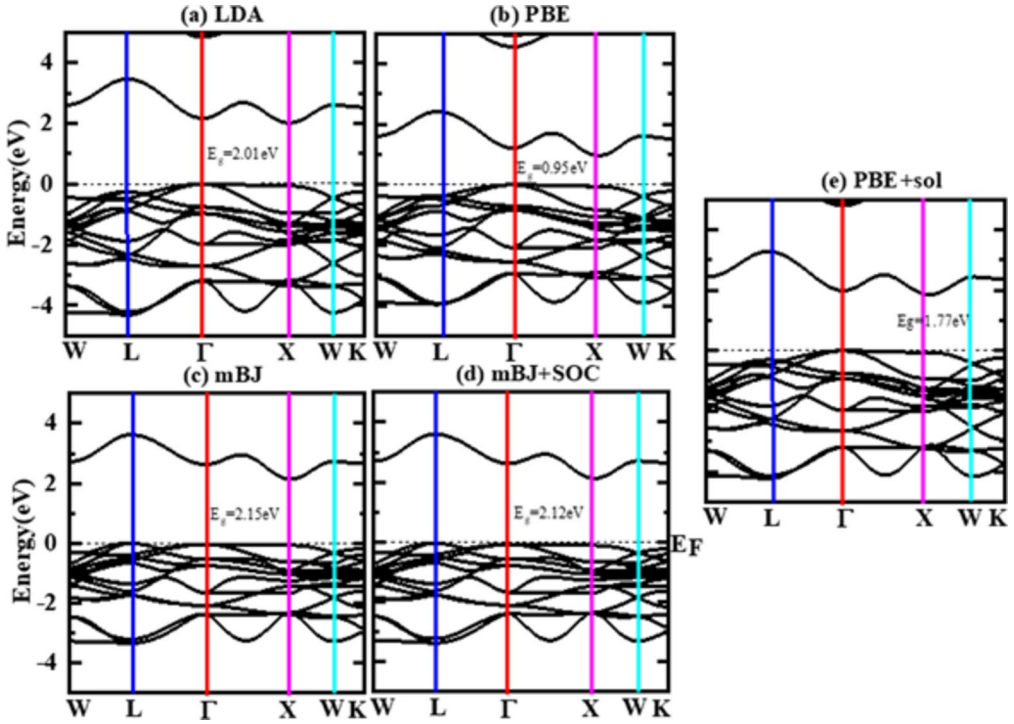

Fig. 4 Electronic band structure diagrams alongwith the high symmetry directions and considering **a** LDA, **b** PBE-GGA, **c** mBJ and **d** mBJ + SOC, **e** PBEsol exchange potentials

We have also calculated total density of states (TDOS) and projected density of states (PDOS) spectra to provide a deep insight for the electronic structure. The PDOS and TDOS of Sr_2YBiO_6 using the TB-mBJ method for energies ranging from − 10 to + 10 eV is shown in Fig. 5. The valence band near to Fermi level i.e., in the range between − 3.500 eV and 0 eV consists of '5p' like states of O and '6p' like states of Bi in Sr_2YBiO_6. The valence bands were formed by merging the Sr-4p, Y-4d, Bi-7s and O-2p orbitals with energies extending from − 7.500 to 0.0 eV. The valence band, vacillating from − 2.600 eV to Fermi level is dominated by the O-2p states. The empty band in the range of 6.100 to 9.970 eV for Sr_2YBiO_6 is dominated by Sr-4d, Y-4d, and Bi-6p states. The lower part of the conduction bands was dominated primarily by '7s' like states of Bi and '2p' like states of O, with a negligible contribution of '4d' like states of Yttrium.

An important tool for examining the localization and dispersion of electrons of a crystalline structure is the charge density profile. Charge density contour provides information about the location of electrons in the lattice space and the bonding properties of materials by quantifying the likelihood of locating electrons with the same spin and established positions inside a reference electron field. The 2D 110 and 101 plane along crystal dimension Charge density maps for the Sr_2YBiO_6 compounds are displayed in Fig. 6(a and b). Lower electron density regions are shown in blue, and greater electron density regions are shown in red on the right side of the contour maps, which show the charge density scaling, including the coordination scaling. The Sr_2YBiO_6 compounds' substantial electronegativity is responsible for the increased level of electron localization around the O ions that was seen in the charge density contour maps analysis. This observation aligns with the results of the examination of Bader charges.

3.3 Optical Properties

Optical properties of the investigated DP Sr_2YBiO_6 give an insight into how the material interact with the incident electromagnetic radiations [18]. The understudy material is in its cubic phase with the isotropy. The dielectric function enlightens us about the interaction of photons and electrons in the material. We have calculated the dielectric function ε(ω) as a tensor, which is a 3 × 3 matrix. For isotropic materials, all diagonal elements are equal, and off-diagonal elements are zero. Since the components of the tensor (e.g., ε_{xx}, ε_{yy}, ε_{zz}) are equal, therefore, properties are expressed in xx direction only. Cohen-Ehrenreich devised an equation which represents dielectric function $\epsilon\ (\omega)$ in a complex form:

$$\epsilon\ (\omega) = \epsilon_1\ (\omega) + i\epsilon_2\ (\omega) \tag{4}$$

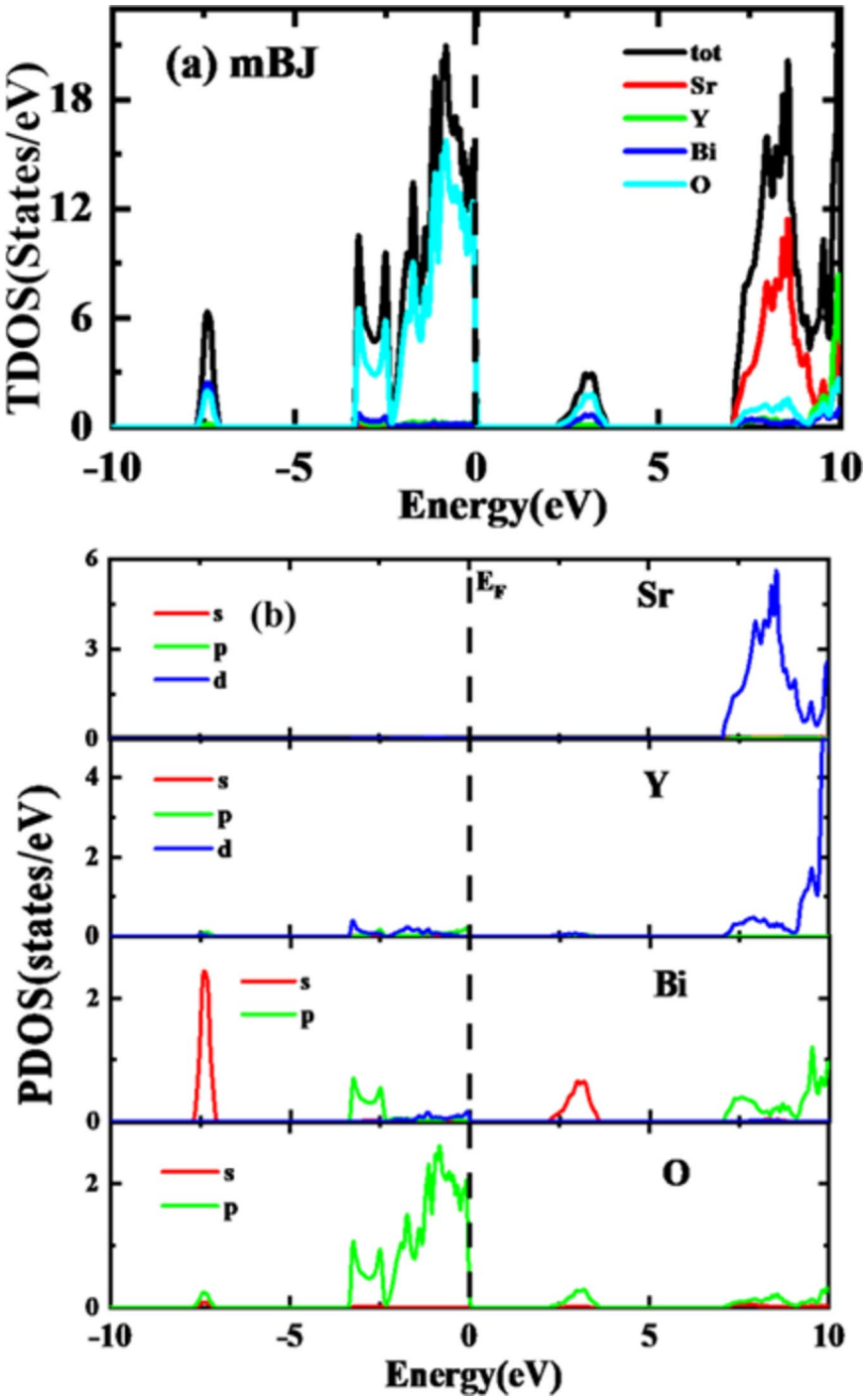

Fig. 5 Density of states plots for Sr_2YBiO_6 compound using mBJ potential **a** total density of states (TDOS), **b** partial density of states (PDOS)

Table 2 Calculated energy bandgap (in eV) by different potentials LDA, PBE, mBJ and mBJ + SOC

Properties	LDA	PBE	mBJ	PBEsol	mBJ + SOC
Sr_2YBiO_6	2.015	0.959	2.150	1.777	2.122
Ref.	1.295 [19] 2.874 [23]	0.922 [19] 1.68 [20] 0.71 [21]	2.147 [19] 1.2 [67] 2.1 [68]	1.156 [19]	3.610 [22] 3.319 [23] 3.952 [24]

In the above equation ω represents angular frequency of the incident electromagnetic radiation. The real part $\epsilon_1(\omega)$ of the complex dielectric function is linked with dispersion as well as electronic polarization, whereas its imaginary part $\epsilon_2(\omega)$ is associated to the optical absorption. Therefore, the $\epsilon_2(\omega)$ spectrum reveals how the electrons get excited from the filled valence band to the unfilled conduction band. The imaginary part of dielectric function, $\epsilon_2(\omega)$ can be inscribed as [69–71].

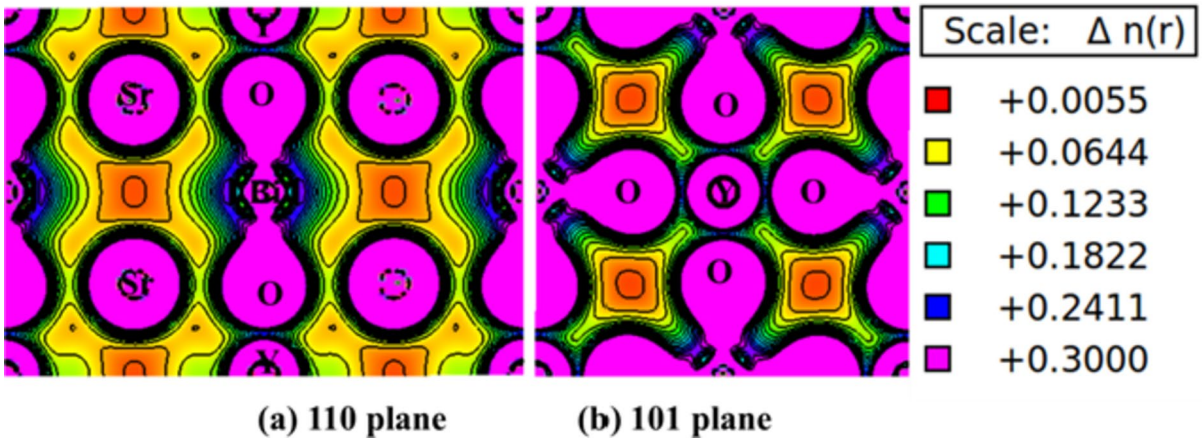

Fig. 6 Charge density contour plots for double perovskite Sr_2YBiO_6 considering **a** 110 plane, **b** 101 plane

$$\epsilon_i(\omega) = \frac{e^2\hbar}{\pi m^2} \sum_{v,c} \int_{BZ}^{\infty} |M_{CV}(k)|^2 \, \delta\,[\omega_{cv}(k) - \omega\,]\, d^3k \tag{5}$$

To determine the real part of the dielectric, below mentioned Kramer-Kronig relation is used.

$$\epsilon_r(\omega) = 1 + \frac{2}{\pi} P \int_0^{\infty} \frac{\omega' \epsilon_i(\omega')}{\omega'^2 - \omega^2} d\omega' \tag{6}$$

Here, P is the principal integral. The Kramer's- Kronig relation has been utilized to compute the real part of dielectric function $\epsilon_1(\omega)$[65].

Optical characteristic quantities, such as extinction coefficient $k(\omega)$, absorption coefficient $\alpha(\omega)$, optical conductivity $\sigma(\omega)$, refractive index $n(\omega)$, reflectivity $R(\omega)$ and energy loss $Eloss(\omega)$ have also been computed. The computed optical characteristics with the incident photonic energy ranging from 0 to 12 eV are illustrated in Fig. 7 (a–e) and Table 3. Figure 7 (a) portrays the imaginary as well as real dielectric constants $\epsilon(\omega)$ as a variable of the incident electromagnetic energy. We have noticed that the investigated DP Sr_2YBiO_6 is isotropic as well as homogeneous, which indicates that the magnitude of its dielectric value is not affected by the orientation of the electric field of the incoming light, although it fluctuates to some amount with the incoming light frequency. The static dielectric constant $_1(0)$ epitomizes the material's dielectric constant and its value is found to be 3.320. It can be seen in Fig. 7 (a) that the magnitude of $\epsilon_1(\omega)$ gradually increases with the incident photon energy with two peaks. The initial dielectric peak $\epsilon_1(\omega)$ occurs around 3.100 eV in the visible region, trailed by additional protruding peak at 7.250 eV in the UV region. Afterwards, it starts to decrease gradually and becomes negative after 10 eV. The material demonstrates metallic behaviour with negative values of $\epsilon_1(\omega)$; otherwise, it is dielectric.

The value of $\epsilon_2(\omega)$ is found to be zero till 2.150 eV, revealing its semiconducting behaviour as seen from Fig. 7(a) and the optimal value of ε_2 (ω) for this compound is found to be in the vicinity of 3.150 eV. The gap between the energy bands (2.150 eV) has been calculated from the electronic band structure, illustrating the accurateness of the obtained results. At this moment, an optical excitation occurs among the lowest conduction and highest valence bands. After this point, the curve rises due to contributing to ε_2 (ω). The protruding two optimal in the spectrum of Sr_2YBiO_6 were at 5.120 eV and 7.280 eV. These peaks originated from electronic excitations from the filled O-2p state to the empty Bi-7s state.

Figure 7(b) also illustrates the refractive index $n(\omega)$ and extinction coefficient $k(\omega)$. $n(\omega)$ gives an insight to the optical feature that gives clear evidence showing the propagation of light through a material. In addition, it determines the absorption capability of the materials. The static refractive index of the compound $n(0)$, is obtained as 1.820 for Sr_2YBiO_6. This graph illustrates that the $n(\omega)$ increases with the incident electromagnetic radiation, with the optimal peak at 3.1 eV. Then it sharply declines with the incident photon energy to attain the low value in the UV region. From Fig. 7 (a) and (b), both $n(\omega)$ and $\epsilon_1(\omega)$ follow the similar trend. The extinction coefficient $k(\omega)$ has been computed Fig. 6(b). It is observed to follow the similar trend as of $\epsilon_2(\omega)$. Next to this, we have computed $\alpha(\omega)$, determines the quantity of incident photon energy riveted per unit thickness of the studied compound. While the absorption coefficient rises, the material becomes more effective in transferring electrons from the occupied bands to the unoccupied bands. The static values are compared with the similar DPs [19, 45, 47] in Table 3.

Figure 7 (d) shows how $\alpha(\omega)$ varies with incident electromagnetic radiation energy. This figure shows several absorption zones spanning from visible to UV region, with

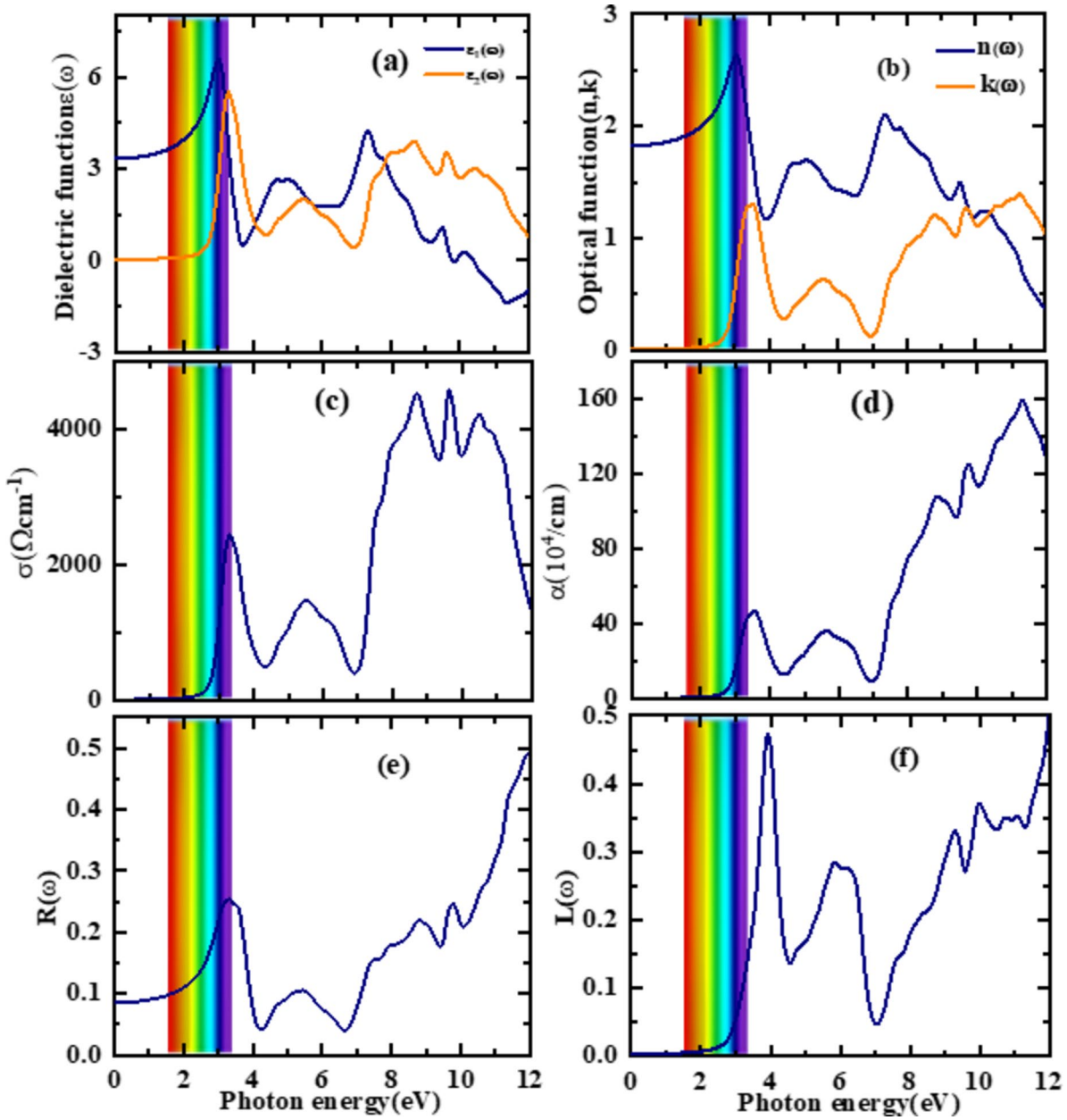

Fig. 7 Optical parameters aspects plots against photon energy for Sr_2YBiO_6 compound. **a** Dielectric function ε, where $\varepsilon_1(\omega)$ (black color) represents real part of ε and $\varepsilon_2(\omega)$ (orange color) represents imaginary part of ε, **b** optical function (n, k), where n(ω) represents refractive index (black color) and k(ω) represents excision coefficient (orange color), **c** optical conductivity σ(ω), **d** absorption coefficient α(ω), **e** reflectivity R(ω), **f** electron loss function L(ω) (Color figure online)

the maximum at 11.520 eV. Besides, the material's absorption edge was 2.150 eV, matching to the indirect changeover among the lowest and highest of the unoccupied and occupied bands, respectively. From Fig. 7(c and d) absorption can be seen zero where $\sigma\ (\omega)$ is found to be zero. We can also notice that when the absorption is at its peak, the $\sigma\ (\omega)$ is maximum. The results have indicated that the Sr_2YBiO_6 compound is suitable for visible-light and UV optoelectronic applications.

The optoelectronic conductivity with incident photon is characterized as $\sigma\ (\omega)$ in Fig. 7 (d) It is found to be zero till 2.150 eV, after which $\sigma\ (\omega)$ of Sr_2YBiO_6 began to rise. The maximum of σ(ω) was attained between 8.0 eV and 10 eV with 4358.2 Ω^{-1-1} in magnitude. Reflectivity in optics refers to the fraction of incident light (or photon energy) that is reflected off a surface rather than being absorbed or transmitted. The refractive index (n=n+ik) is frequency-dependent, where: n (real part) determines phase velocity, k (imaginary part, extinction coefficient) determines

Table 3 Calculated optical and transport properties of Sr2YBiO6 using mBJ-GGA potential at 300 K

	Material property	Sr_2YBiO_6	Other work
Optical properties	$\varepsilon_1(0)$	3.320	3.420 [19] 2.460 [45]
	R(0)	0.085	0.084 [19] 0.054 [45] 0.07 [45]
	$n(0)$	1.820	1.840 [19] 1.710 [47]
Transport properties (300 K)	$\sigma/\tau(10^{18}\Omega^{-1}m^{-1}s^{-1})$	1.591	1.680 [45]
	S(μV/K)	214.800	243 [19]
	κ_L (W/mK)	1.561	2.240 [19]
	κ_E (10^{15}W/mKs)	0.143	0.100 [19]
	κ_{tot} (10^{15}W/mKs)	1.704	2.350 [19]
	$S^2\sigma/\tau(10^{12}W/K^2ms)$	0.734	~0.400 [47]
	ZT	0.064	0.75 [19] 0.15[45]
	Debye temperature	422.200	443.30 [49]
	charge carrier concentration (e/uc)	0.112	–

absorption. When photon energy matches the bandgap of a material, absorption increases, reducing reflectivity. Reflectivity spectrum $R(\omega)$ is illustrated in Fig. 7 (e). We computed reflectivity at zero frequency $R(0)$ to be 8.50% as seen from this Fig. 7 (e), which means 8.5% of incident light is reflected. The optical $R(\omega)$ value increased with the radiation energy. The maximum value of $R(\omega)$ was almost 49.50% in the UV region at 12.0 eV. Though, the compound's $R(\omega)$ value was 1% in the energy gap range. The material confirmed transparent nature for incident photon energy till bandgap energy, suggesting that the Sr_2YBiO_6 is apt for lens manufacture. Figure 7 (f) illustrates the photonic response of electron loss function (ELF) $L(\omega)$. $L(\omega)$ is a crucial component in determining the loss of energy of electron as it traverses through the material. The ELF peaks at the plasmon frequency, which corresponds to the collective oscillations of free electrons in a material. Peaks in the ELF also arise due to transitions between electronic energy bands, providing insights into the band structure. A sharp increase occurs around 2 eV, indicating a significant optical transition or absorption edge. Several peaks appear at different energy levels (e.g., around 4 eV, 6 eV, 8 eV, and 10+eV), likely corresponding to electronic transitions in the material. The rainbow-colored band (ranging from red to violet) on the left side (around 1.5–3 eV) suggests that this portion of the spectrum corresponds to the visible light range. The sharp increase near 2 eV indicates the material's optical bandgap, beyond which it begins interacting strongly with light. The sharp rise at ~2 eV could be the plasma resonance or an interband transition.

3.4 Thermoelectric Properties

Due to the energy consumption as well as substantial heat losses, researchers are intrigued in assessing novel compounds and developing techniques for adapting thermal into electrical energy [19–22]. Several features impede this search for novel substances which possess an excellent thermal energy into electrical energy transformation aspect, are effortlessly readily available plentiful in nature, less expensive, and configurable for acceptable qualities [23, 24]. The material's energy band gap is best evaluated using the TB-mBJ technique. As a result, the thermoelectric characteristics have been evaluated with BoltzTraP package [72] depending on the computed TB-mBJ band plot.

The temperature dependence of transport properties like Seebeck coefficient (S), power factor ($\mathrm{PF} = \sigma S^2/\tau$), figure of merit $(\mathrm{ZT} = S^2\sigma T/\kappa)$, electrical conductivity (σ/τ) have been studied in the range of 0 to 1200 K and presented in Fig. 8 (a)– (e). The Seebeck coefficient denoted by *S*, which is computed as the potential temperature gradient between different metallic contacts. The positive value of S indicates the p-type nature of the investigated DP, which again align with that we observed in band structures also. The variation of S with temperature is depicted in Fig, 8(a). The value of S at 300 K is $214\mu V/K$ and tabulated in Table 4. The Seebeck coefficient is found to be decreasing with increasing temperature. We have estimated power factor value for the studied material and its variation with temperature is presented in Fig. 8(b). Our estimated value is 0.734×10^{12} W/K^{2}ms, which is in agreement with the other DPs [47]. The electrical conductivity σ/τ and thermal conductivity κ/τ of the investigated compound have been studied with the temperature. The thermal conductivity κ

$$\kappa = \kappa_e + \kappa_l \tag{7}$$

where κ_e-electronic thermal conductivity and κ_l- lattice thermal conductivity [44].

Electrical conductivity of the studied DP is found to be increasing (Fig. 8(c)) whereas thermal conductivity increases with the temperature (Fig. 8(e)). The increase in electrical conductivity with temperature confirms its semiconducting nature. BoltzTraP can compute only electronic part of thermal conductivity, and doesn't support for lattice part. Therefore, we have computed the lattice part of thermal conductivity using the Slack equation [73] relation.

$$\kappa_l = A.\frac{M\theta_D^3\delta}{\gamma^2 T n^{\frac{2}{3}}} \tag{8}$$

Where M- total molecular mass, A- constant, n- number of atoms in the unit cell, δ – atomic volume, T - absolute

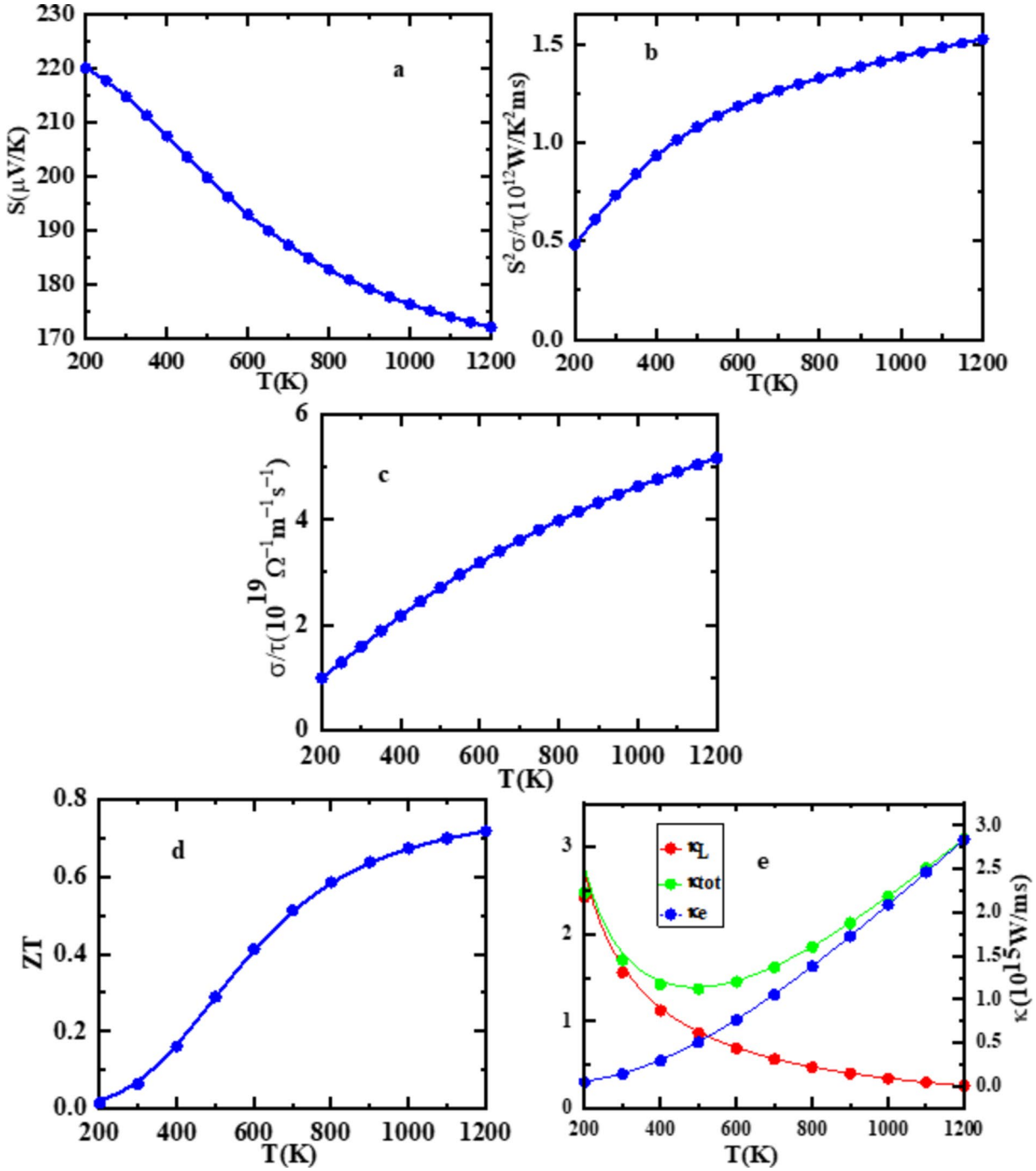

Fig. 8 Variation of thermoelectric properties against temperature (0–1200 K). (a) Seebeck coefficient S (b) power factor with relaxation time τ, $S^2\sigma/\tau$ (c) electrical conductivity with relaxation time τ, σ/τ (d) figure of merit, ZT (e) thermal conductivity κ, where κ_L represents lattice thermal conductivity, κ_e represents electronic thermal conductivity and κ_{tot} represents overall thermal conductivity

temperature, γ - Gruneisen parameter, θ_D – Debye temperature. The thermal dependence of κ_e, κ_l and κ_{tot} has been studied and displayed in Fig. 8 (e). It is found that κ_e increases with temperature whereas κ_l decreases. In the low temperature region, κ_{tot} decreases and it increases steadily after 600 K. Figure of merit ZT is one of the critical parameters in determining the thermoelectric capability of the material. As observed in Fig. 8 (d), ZT increases with the temperature, which shows it is a promising candidate for thermoelectric applications. Our calculated thermoelectric parameters are summarized and compared with the similar double perovskite oxides [19, 45, 47, 49] in Table 3.

The double perovskite Sr_2YBiO_6 is thoroughly explored in regards to thermoelectric features like power factor

Table 4 Calculated values of elastic constants (C_{ij}), bulk modulus (B), shear modulus (G), Young's modulus (E), Poisson's ratio (σ), Pugh ratio, Frantsevich ratio, shear anisotropy factor (A) cauchy pressure C^P, sound velocities (m/s), Debye temperature Θ_D (K) of double perovskite Sr_2YBiO_6 at 0GPa and 0 K

Material property	Sr_2YBiO_6	Other work
C_{11} (GPa)	227.705	170.410 [49]
C_{12}(GPa)	55.270	56.570 [49]
C_{44}(GPa)	51.7343	69.500 [49]
Bulk modulus, B (GPa)	112.747	94.520 [49]
Shear modulus, G (GPa)	63.557	64.160 [49]
Young modulus, E (GPa)	160.510	156.960 [49]
Poisson ratio, σ (GPa)	0.262	0.223 [49]
Pugh ratio, B/G (GPa)	1.770	1.470 [49]
Frantsevich ratio, G/B(GPa)	0.560	0.680 [49]
Shear anisotropy factor, A (GPa)	0.600	0.891 [47]
Cauchy pressure C^P (GPa)	3.530	6.13 [47]
Transverse sound velocity (m/s)	3277.170	3280.510 [49]
Longitudinal sound velocity(m/s)	5776.830	5495.810 [49]
Average sound velocity (m/s)	3643.770	3630.86 [49]
Debye Temperature Θ_D (K)	430.788	443.30 [49]
Melting temperature T_m(K)	1898.738	1560±300 [49] 2223±300 [47]

(PF), figure of merit (ZT), thermal conductivity (κ/τ), electrical conductivity (σ/τ), and S with $\mu - \epsilon_F$ at 300, 700, and 1200 K under this study is shown in Fig. 9 (a–e). The dashed lines showed that the Fermi level was zero energy, as shown in Fig. 5. The electron-doped zone (n-type doping) and the hole-doped region (p-type doping) have positive and negative $\mu - \epsilon_F$ values, respectively. Figure 9 (a) illustrates that when the temperature rises from 300 to 1200 K, the peaks decrease and shift towards higher chemical potential values. One can see from the Fig. 9 (a) that the optimal value of S for the solid was accomplished in the positive $\mu - \epsilon_F$ at about of 3100.500 μV/K at 300 K. S was approximately 214.800 $\mu V/K$ for DP Sr_2YBiO_6 at $\mu - \epsilon_F = 0$ (Fermi level). The positive number indicates that most charge carriers are holes, implying that the Sr_2YBiO_6 compound is p-type semiconductor.

Figure 9 (b) displays an illustration of electrical conductivity (σ/τ) vs. $\mu - \epsilon_F$ demonstrating that the material's σ/τ was negligible in the chemical potential region linked with the bandgap energy. The optimal value of σ was obtained due to p-type doping at higher potential chemical values. The value of σ increases from origin to an optimal value of $2.75 \times 10^{20}\ \Omega^{-1} m^{-1} s^{-1}$ at −0.95 eV. The transport distribution function or DOS affects the value of σ, not temperature. Hence, it is found that σ is found to be constant with the temperature for the double perovskite Sr_2YBiO_6 compound [74–76]. The electronic thermal conductivity (κ_e/τ), and electronic conductivity (σ) were measured in the hole-doped region of the Sr_2YBiO_6 compound, as shown in Fig. 9 (c). The electronic thermal conductivity (κ_e/τ), like the electronic conductivity (σ/τ), was obtained in the holes-doped region for the Sr_2YBiO_6 compound as in Fig. 9 (c). The chemical potential dependence of figure of merit ZT has been studied and plotted in Fig. 9(d). ZT approaches almost 1.0 in the range of 0 to 2.0 eV. The carrier concentration dependence of thermoelectric parameters like power factor, figure of merit, electrical and thermal conductivity of studied DP Sr_2YBiO_6 compound and presented in Fig. 9(d and e).

We computed the effective mass for electron and hole to gain an understanding of charge carrier movement.

$$m^*_{e.a} = \left[\frac{1}{\hbar^2}\frac{\partial^2 E_{CBM}(k)}{\partial k_a^2}\right]^{-1},\ m^*_{h.a} = \left[\frac{1}{\hbar^2}\frac{\partial^2 E_{VBM}(k)}{\partial k_a^2}\right]^{-1} \tag{9}$$

where the eigen energies versus wave number vector k at conduction band minima (CBM) and valence band minima (VBM) are ECBM (k) and EVBM(k), correspondingly, and the Cartesian component is denoted by (α=x, y, z). or the situations of DPs, it was discovered that the effective mass vectors, computed at the Γ point of BZ, were somewhat anisotropic for holes $m^*_{h,x} = m^*_{h,y}\, m^*_{h,z}$ but isotropic for electrons $m^*_{e,x} = m^*_{e,y} = m^*_{e,z}$. For the electron and hole estimated at the Γ and X locations, correspondingly, they were totally anisotropic $m^*_{h,x}\ m^*_{h,y}\, m^*_{h,z}$. The unusually heavy hole in the Sb-based perovskites along the X (1/2, 0, 1/2), L (1/2, 1/2, 1/2) line in the Brillouin zone is the primary cause of the hole effective mass's high anisotropy. It is evident that the effective masses of holes and electrons are greater for both DPs [77, 78]. In Fig. 10, we have presented variation of thermoelectric parameters as a function of carrier concentration. Figure 10(a) Seebeck coefficient, Fig. 10(b) power factor with relaxation time τ, $S^2\sigma/\tau$ Fig. 10(c) electrical conductivity with relaxation time τ, σ/τ Fig. 10(d) electronic thermal conductivity κ_e and Fig. 10 (e) electronic figure of merit, ZT_e. The graph includes data for three different temperatures: Blue line for 300 K, Orange line for 700 K, Cyan line for 1200 K. The Seebeck coefficient changes sign Fig. 10(a), which suggests that both electrons and holes contribute to transport at different energy levels.

From Fig. 10(c), it can be understood that the conductivity varies with carrier concentration. There is a minimum near $N=0$, suggesting a low carrier density leads to minimal conductivity. As N increases positively or negatively, the conductivity increases.The differences between the curves suggest temperature dependence, with higher temperatures leading to slight variations in conductivity. However, importantly, Fig. 10(e) expresses at higher temperatures (e.g., 1200 K), the peak value of ZT_e is slightly reduced compared to lower temperatures. The drop-off in ZT_e at large positive and negative N values suggests that excessive doping may degrade thermoelectric performance. The

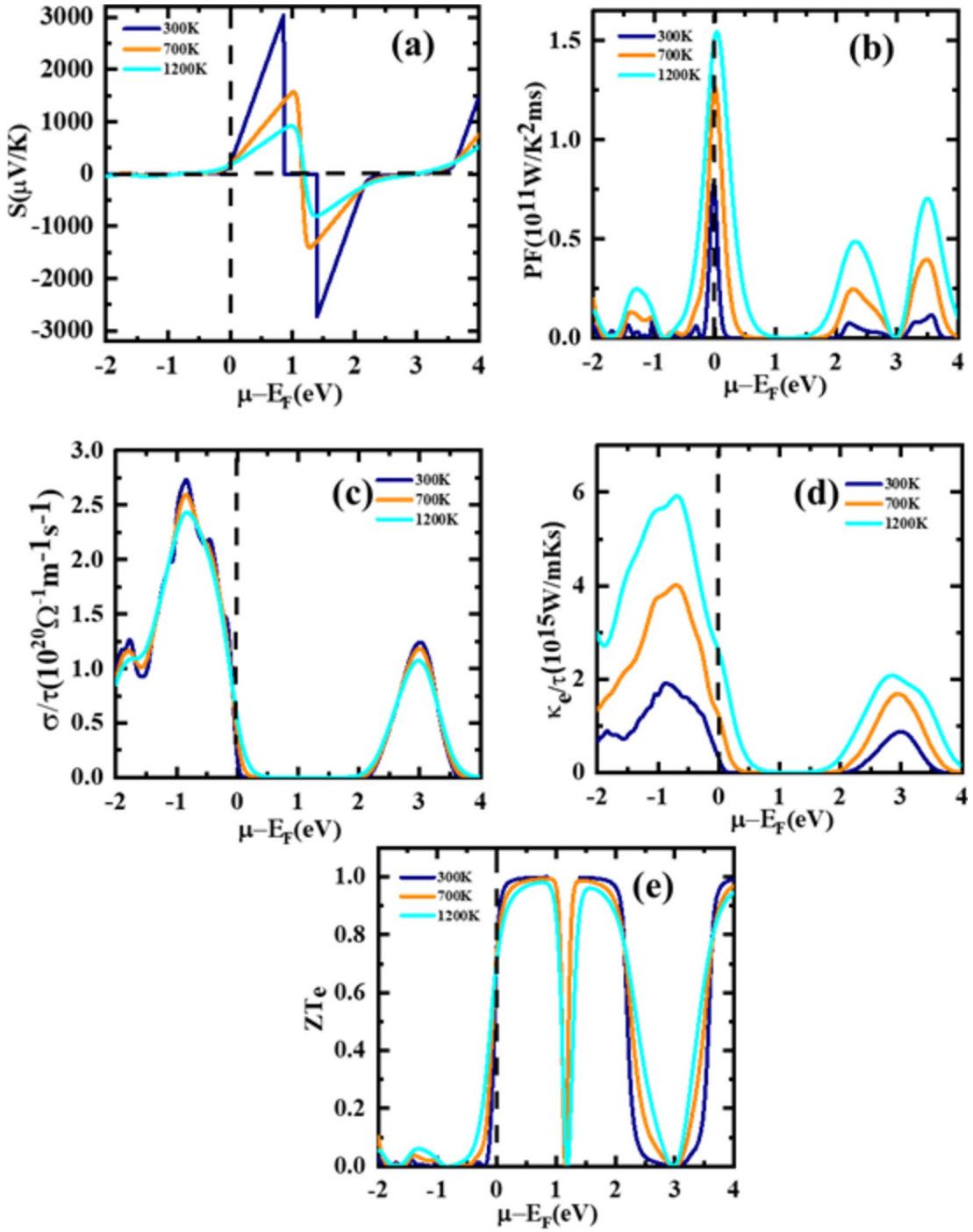

Fig. 9 Variation of thermoelectric parameters versus chemical potential. **a** Seebeck coefficient S, **b** power factor, PF, **c** electrical conductivity with relaxation time τ, σ/τ, **d** electronic thermal conductivity κ_e with relaxation time τ, **e** electronic figure of merit, ZT_e

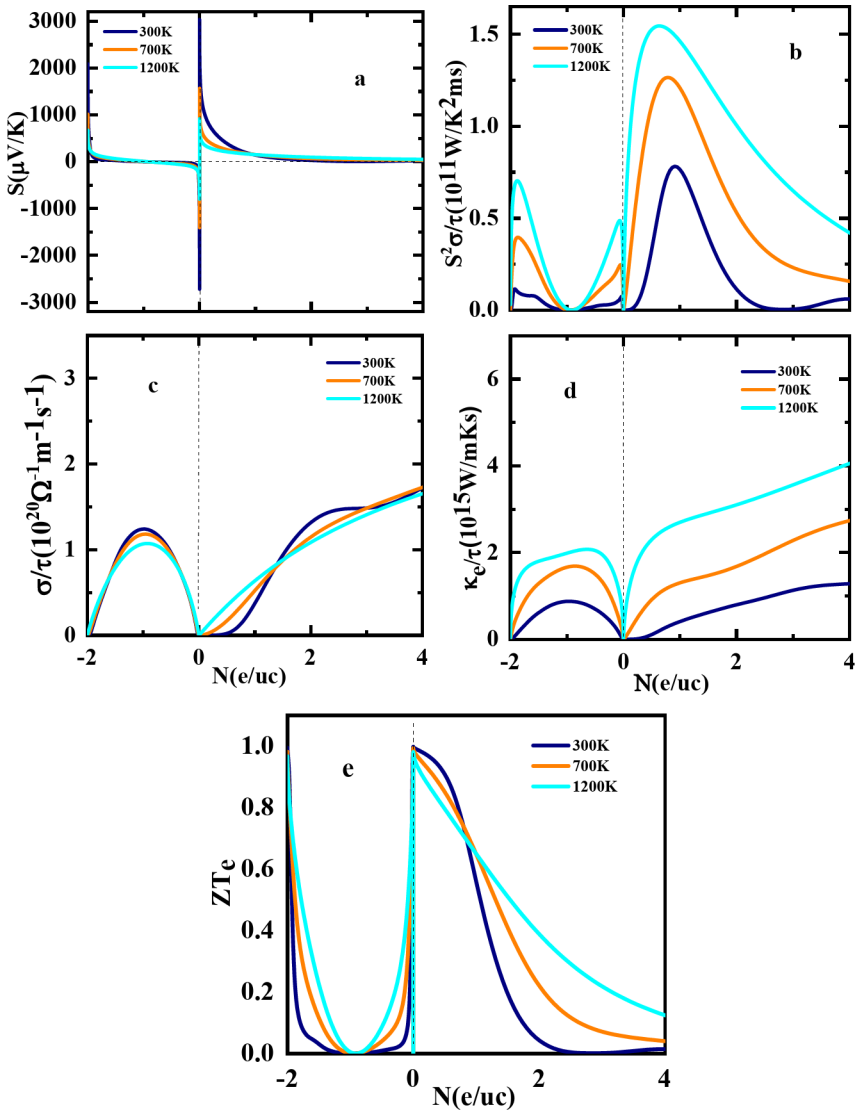

Fig. 10 Variation of thermoelectric parameters as a function of careeir concentration. **a** Seebeck coefficient, S **b** power factor with relaxation time τ, $S^2\sigma/\tau$, **c** electrical conductivity with relaxation time τ, σ/τ, **d** electronic thermal conductivity, κ_e, **e** electronic figure of merit, ZT_e

dependence on temperature suggests that optimizing doping levels and operating temperatures is crucial for maximizing thermoelectric efficiency.

3.5 Thermodynamic Properties

The thermodynamic behavior of the double perovskite Sr_2YBiO_6 has been studied with Gibb's2 software [79], that depends semi empirical quasi harmonic Debye theory in the range 0 to 400 K & pressure up to 111 GPa and presented in Fig. 11 (a)–(f). The volume of the compound is found to increase with temperature and decrease with the pressure as observed in Fig. 11 (a). The increase in kinetic energy at high temperatures generates higher zig-zag movement for thermally produced carriers, and compounds can be shrunken more quickly, ending in a decreased relative volume at a particular pressure. As seen from Fig. 11 (b), bulk modulus is found to be constant in the low temperature region and slightly decreasing in the high temperature region and its value increases with the pressure. Therefore, we can conclude that at a particular pressure, compressibility ($1/B$) is constant with temperature. At the same temperature, compressibility diminishes with rising pressure [80–82]. As the pressure increases, the compression coefficient gets decreased. It can be countered by increasing the temperature, thus reducing the effect of rising pressure. This outcome indicates that the cubic double perovskite Sr_2YBiO_6 displays brilliant compression resistance even when exposed to high pressure. Specific heat capacity C_V is found to be increasing in the low temperature region whereas it attains a constant value (~250 J/mol·K), obeying Dulong Petit's law, as seen in Fig. 11 (c). Each curve corresponds to a different pressure level, ranging from 0 GPa to 110 GPa. Higher pressures tend to reduce heat capacity at lower temperatures but still follow a similar saturation trend at high temperatures. The effect of pressure is significant at lower

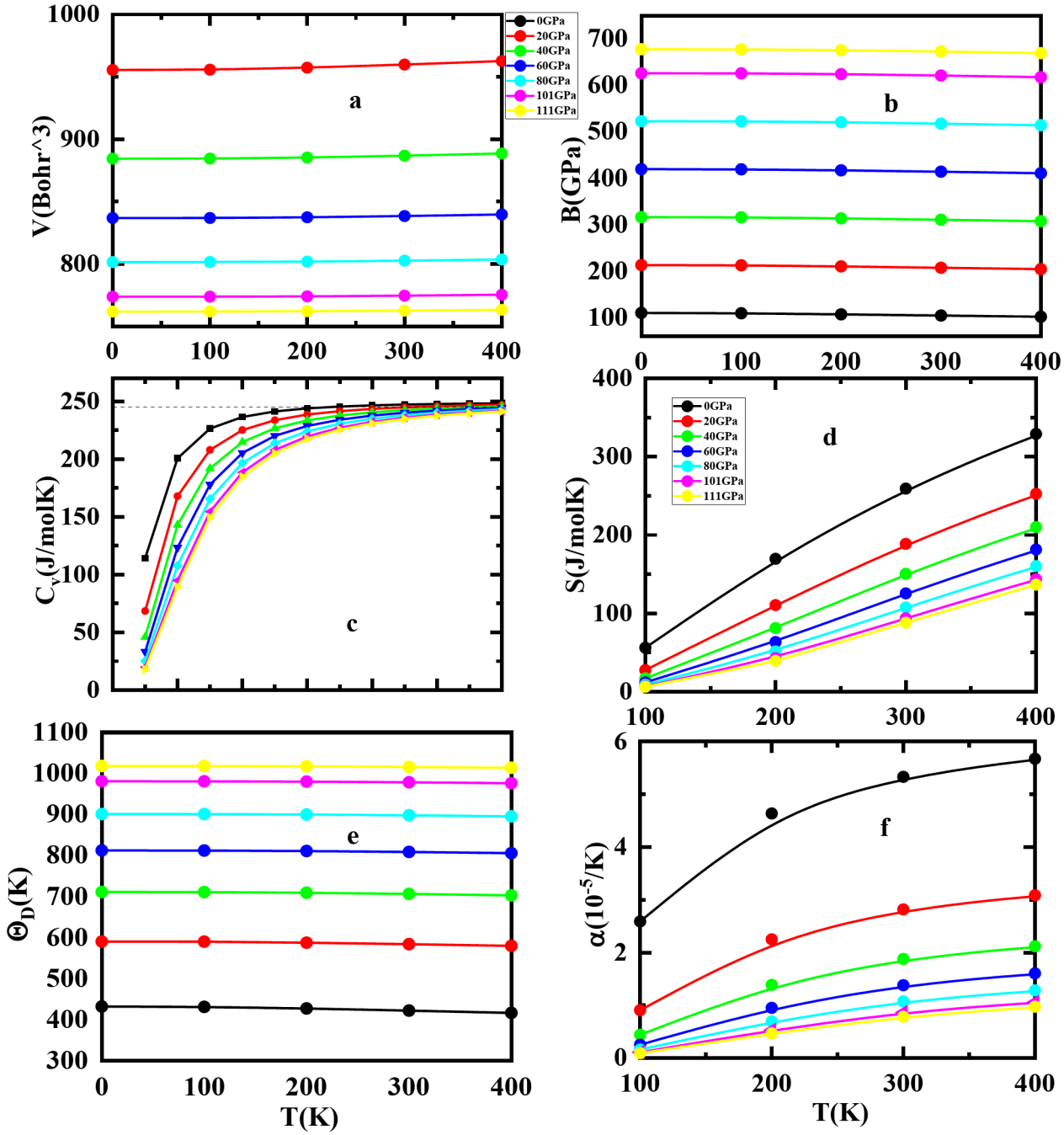

Fig. 11 Variation of thermodynamics parameters against temperature at varying pressure (0GPa- 111GPa) for Sr_2YBiO_6. **a** Unit cell volume V, **b** bulk modulus B, **c** heat capacity at constant volume C_v, **d** entropy S, **e** Debye temperature θ_D, **f** absorption coefficient α

temperatures but diminishes at higher temperatures where all curves tend to a similar asymptotic value. This behavior is typical of many solids, where vibrational modes dominate heat capacity at low temperatures, and classical limits are reached at high temperatures. Entropy S, which measures the degree of disorderness in the system, has also been studied with temperature and pressure and illustrated in Fig. 11 (d). Entropy is also found to increase with the temperature while decreasing with the pressure. Debye temperature θ_D gives an insight on the amount of dynamic distortion applicable to the crystal lattice. Numerous physical qualities of the materials are related with it, including elasticity, melting point, and heat capacity etc [82–84]. The temperature as well as pressure dependence of θ_D has been studied and illustrated in Fig. 11 (e). We report its value 430.788 K at 0 GPa and 0 K. The different colored curves likely correspond to different pressure values, each maintaining a relatively constant Debye temperature across the temperature range.

The nearly horizontal lines suggest that the Debye temperature does not significantly change with increasing temperature for these cases. A Debye temperature of 438–788 K for Sr_2YBiO_6 suggests that its lattice vibrations are frozen out (quantum effects dominate) at much lower temperatures. It would be worth to mention that at temperatures below θ_D, the heat capacity (C_v) follows a T^3 dependence (Debye's law), while above θ_D, it approaches the classical Dulong-Petit limit (constant heat capacity).

The coefficient of thermal expansion α, displays structural stability of materials. The temperature as well as pressure dependence of thermal expansion coefficient (α) is depicted in Fig. 11 (f). It increases rapidly up to 200 K, after becomes almost constant in the higher temperature region. This could be because, due to electronic contributions, Sr_2YBiO_6's thermal expansion coefficient is unaffected by temperature rise. At 0 GPa (black curve), the thermal expansion coefficient is highest and increases significantly with temperature. As pressure increases (red, green, blue, etc.), the values of α decrease. At the highest pressure (111 GPa, yellow curve), α is the lowest and shows minimal variation with temperature. Therefore, elevating both temperature and pressure has the opposite impact on thermal expansion. The graph suggests that applying higher pressure suppresses the thermal expansion of the material. This is a common phenomenon in many materials, where increased pressure limits atomic vibrations and lattice expansion.The thermodynamic behavior obtained for the studied DP is in well agreement with the similar reported DPs.

3.6 Elastic Properties

In this section, we have also studied the elastic properties of the investigated DP Sr_2YBiO_6, which aids in understanding the crucial information about the material that can give an insight into knowing about its effect on design and applications in the field of technological as well as industrial field. We have computed them with the help of IRelast software [85], which is incorporated with the WIEN2k code and the obtained results are tabulated in Table 4. The studied DP Sr_2YBiO_6 is found to be mechanically stable as it satisfies Born's criteria i.e.,

undefined

$$C_{11} > 0,\ C_{44} > 0,\ (C_{11} - C_{12}) > 0,\ C_{12} < B < C_{11} \tag{10}$$

The following relations can be used to find mechanical properties of the compounds, like the bulk modulus B, Young's modulus E, shear modulus $G_v, G_R,\ G$ and anisotropy factor A.

$$B = \frac{C_{11} + 2C_{12}}{3} \tag{11}$$

$$E = \frac{9BG}{3B + G} \tag{12}$$

$$G_v = \frac{C_{11} - C_{12} + 3C_{44}}{5} \tag{13}$$

$$G_R = \frac{5C_{44}(C_{11} - C_{12})}{4C_{44} + 3(C_{11} - C_{12})} \tag{14}$$

$$G = \frac{G_v + G_R}{2} \tag{15}$$

$$A = \frac{2C_{44}}{C_{11} - C_{12}} \tag{16}$$

In order to get an insight into how the materials resist to compression as well as rigidity, we have calculated bulk modulus with the help of computed second order elastic constants and tabulated in Table 4. The calculated value of B from elastic constants is found to be 112.747 GPa, which is slightly less than that got from volume optimization method. Similarly, we have computed the shear modulus value of 63.557 GPa. This indicates how much the material's resist to shear deformation on application of parallel external forces. We have also evaluated Young's modulus that quantifies stiffness of materials by depicting its response to tensile-stress and Poisson's ratio which defines the ratio of lateral strain to axial strain, when a material undergoes expansion or compression. The Sr_2YBiO_6 gives a value of 160.510 GPa for E and 0.262 for σ. The ductility or brittle nature of the compounds can be assessed with the help of Pugh's ratio, Frantsevich's ratio and Cauchy's pressure. In accordance with Pugh's criterion, if the value of $\frac{B}{G} > 1.75$,undefined1.75,]]> the material exhibits ductile behavior otherwise brittle. As per Table 4, this compound has $\frac{B}{G}$ value of 1.77, which indicates its ductile nature. Frantsevich's ratio, G/B is found to be 0.56, which again reconfirms its ductility.

Cauchy's pressure $C^P = C_{12} - C_{44}$, also tests the ductility/brittleness of the materials. Positive value of it demonstrates ductile nature, otherwise brittle. Positive value of C^P indicates the studied compound's ductile nature. We also calculated the shear anisotropy factor, which is an estimate of how the shear modulus changes with direction in a crystal. It is particularly helpful for cubic crystals and determines how anisotropic (direction-dependent) a material's mechanical properties are. From Table 4, we can see that DP Sr_2YBiO_6 has a value of 0.60 indicates that the studied

compound is anisotropic in nature, and these findings are in well agreement with the reported similar compounds [47, 49].

We have also computed the longitudinal velocity (v_l), transverse velocities (v_t) and average velocity from the below mentioned expressions [70].

$$v_l = \sqrt{\frac{3B + 4G}{3\rho}} \tag{17}$$

$$v_t = \sqrt{\frac{G}{\rho}} \tag{18}$$

$$v_m = \left[\frac{1}{3}\left(\frac{2}{v_l^3} + \frac{1}{v_l^3}\right)\right]^{-(1/3)} \tag{19}$$

To compute the maximum possible temperature value of crystal under normal vibration model, Debye temperature is calculated

$$\theta_D = \frac{\hbar}{k_B}\left[\frac{3n}{4\pi}\left(\frac{N_A\rho}{M}\right)\right]^{-(1/3)} V_m \tag{20}$$

where terms N_A, k_B, $\hbar$, ρ represent Avogadro number, Boltzmann constant, Planck's constant and density, respectively. The relation between the elastic properties of the solids with their thermodynamic features could be understood by Debye temperature such as smelting point, specific heat, vibrational entropy etc., making it a vital parameter [86, 87]. The calculated values of these elastic constants can be seen in Table 4. Debye hardness, also the hardness of solids can be explained by Debye temperature [87–90].

Melting point T_m is correlated to both bonding energy and thermal expansion of crystalline materials. Materials with lower thermal expansion, higher cohesive energy, higher bonding energy and strong atomic interaction have higher melting points [51]. In addition, melting point of compounds or element can be used to predict the temperature up to which the materials are functional without excessive distortion or changes in chemical composition or undergoing substantial oxidation [91, 92]. The melting point T_m of the material in the current study were predicted by the following equation [52]:

$$T_m\,(K) = [553\,(K) + (5.911)\,C_{12}]\,GPa \pm 300\,K$$

The predicted melting point of Sr_2YBiO_6 is 1898.738 ± 300 K using GGA-PBE was used, and these findings imply that it is a suitable material for high-temperature applications. The melting point was treated as a rough estimate since there is a large uncertainty (± 300 K) and there is no experimental value available at present to compare [86, 87].

4 Conclusion

The present work predicts several basic properties such as crystal structure, band plots, including some application properties like optical as well as thermoelectric properties of the double perovskite Sr_2YBiO_6 compound. The same were explored within the framework of (DFT) and BoltzTraP calculations. The calculated electronic properties showcase Sr_2YBiO_6 belongs to p-type semiconductor-family possessing an indirect energy-gap of 2.150 eV along Γ-X direction. The optical characteristics described indicate that the studied material responds actively in the UV and visible part of electromagnetic spectrum. Finally, the thermoelectric properties of Sr_2YBiO_6 were evaluated, with prominent values for figure of merit as well as power factors, which are prominent factors to check the suitability in thermoelectric applications. With the aid of Slack's equation, we found an exceptionally low lattice thermal conductivity of 0.50Wm^(-1) K^(-1) at 1200 K. ZT value of 0.06385 is achieved at room temperature, for the studied DP. At 300K, the value of Seebeck coefficient and power factor have been computed as 214.8 µVK^(-1) and 0.73423 × 〖10〗 ^12 µW cm^{-1} K^{-2}, respectively. Elastic as well as thermodynamic properties are also investigated for this compound. These investigations of Sr_2YBiO_6 were presented for the very first time in this paper, thus they may be beneficial as points of reference for the forthcoming theoretical and experimental prospectus.

Acknowledgements The authors present their appreciation to King Saud University for funding this research through Researchers Supporting Program number (RSPD2025R993), King Saud University, Riyadh, Saudi Arabia.

Author Contributions All persons who meet authorship criteria are listed as authors, and all authors certify that they have participated sufficiently in the work to take public responsibility for the content, including participation in the concept, design, analysis, writing, or revision of the manuscript.Aparna Dixit, Arti Saxena, Mumtaz Manzoor, Sadaf Sahid, Ramesh Sharma- Conceptualization, Methodology, Investigation, formal analysis, Software, Writing- Original draft preparation, Supervision.Ahmed Ahmed Ibrahim, Mohammad A. El-Meligy, Barno Abdullaeva, Vipul Srivastava - Writing- Original draft preparation, Visualization, Investigation. Writing- Reviewing and Editing, funding acquisition.

Data Availability No datasets were generated or analysed during the current study.

Declarations

Competing Interests The authors declare no competing interests.

References

1. J.A. Abraham et al., A comprehensive DFT analysis on structural, electronic, optical, thermoelectric, SLME properties of new double perovskite oxide Pb2ScBiO6. Chem. Phys. Lett. **806**, 139987 (2022)
2. D. Bendjebbour et al., Half-metallic ferrmagnetism in non-magnetic double perovskite oxides Sr2MSbO6 (M=Al, Ga) doped with C and N. Philosoph. Magaz. **103**(2), 186–201 (2023)
3. M. Caid et al., A density functional theory exploration of Cs2B′ B ″I6 (B′ B ″: BeCa, BeSr, GeCd, GeBe, GeMg) Halide double Perovskites for optimal solar cell and renewable energy applications. Physica Status Solidi (b). p. 2300577
4. M. Caid et al., Structural, elastic, electronic, and optical properties of lead-free halide double perovskites Cs2B'B"Br6 (B'B' ': BeMg, CdBe, CdGe, GeMg, GeZn, MgZn): Ab initio calculations. J. Mol. Model. **30**(3), 1–14 (2024)
5. R. Chaurasiya et al., Cation modified A2 (Ba, Sr and Ca) ZnWO6 cubic double perovskites: a theoretical study. Comput. Condens. Matter. **14**, 27–35 (2018)
6. N. Erum et al., DFT insights of mechanical, optoelectronic and thermoelectric properties for Cs2ScTlX6 (X=Cl, Br, I) double perovskites. Opt. Quant. Electron. **55**(4), 337 (2023)
7. M.H. Fahim et al., A comprehensive DFT study of the optoelectronic, mechanical, and thermoelectric properties of Rb2NaScCl6 double perovskite implying different pressures. Mater. Today Commun. **38**, 108093 (2024)
8. Z. Gao et al., High throughput screening of promising lead-free inorganic halide double perovskites via first-principles calculations. Phys. Chem. Chem. Phys. **24**(5), 3460–3469 (2022)
9. M.W. Iqbal et al., DFT insights on the opto-electronic and thermoelectric properties of double perovskites K2AgSbX6 (X=Cl, Br) via halides substitutions for solar cell applications. Mater. Sci. Engineering: B **290**, 116338 (2023)
10. M.W. Iqbal et al., Tuning of the electronic bandgap of lead-free double perovskites K2AgBiX6 (X=Cl, Br) for solar cells applications and their thermoelectric characteristics. Sol. Energy. **239**, 234–241 (2022)
11. M. Ishfaq et al., DFT investigation of optoelectronic and thermoelectric features of Ba2Ce (Sn, Pt) O6 double perovskites. Mater. Chem. Phys. **321**, 129493 (2024)
12. S. Jamshaid et al., Investigation of cubic K2NaXBr6 (X=Sc, Y) double perovskites for optical and thermoelectric devices. J. Phys. Chem. Solids. **178**, 111341 (2023)
13. J. Kangsabanik et al., Double perovskites overtaking the single perovskites: A set of new solar harvesting materials with much higher stability and efficiency. Phys. Rev. Mater. **2**(5), 055401 (2018)
14. M.Z. Kazim et al., Lead-free silver-indium based halide double perovskites for energy harvesting applications. J. Phys. Chem. Solids. **185**, 111756 (2024)
15. M. Manzoor et al., Comprehensive first principles to investigate optoelectronic and transport phenomenon of lead-free double perovskites Ba2AsBO6 (B Nb, Ta) compounds. Heliyon **10**(9) (2024)
16. M. Manzoor et al., Probing direct bandgap of double perovskites Rb2LiTlX6 (X=Cl, Br) and optoelectronic characteristics for solar cell applications: DFT calculations. J. Mater. Res. Technol. **18**, 4775–4785 (2022)
17. A. Kumari et al., Exploring K_2MAuI_6 (M=Sc, Y) double perovskite halides for solar cells: insights from DFT-Based investigations. J. Inorg. Organomet. Polym. (2024). https://doi.org/10.1007/s10904-024-03375-y
18. A. Kumari et al., Exploring the physical properties of novel double perovskites A2InAsO6 (A=Sr, Ba) for renewable energy applications: Ab-initio calculations. Solid State Commun. Volume. **392**, 115654 (2024)
19. S.K. Singh et al., Unveiling the energy driven potential Sc-based double perovskite through comprehensive DFT screening on physical, optoelectronic and transport characteristic of Sr2ScAsO6 compound. Solid State Commun. Volume. **394**, 115676 (2024)
20. A. Nazir et al., Impact of halogens modifications on physical characteristics of lead-free hybrid double perovskites compounds Cs2YCuX6 (X = Cl, Br, and I) for energy storage applications: first principles investigations. Chem. Phys. **588**, 112449 (2025)
21. A. Nazir et al., Theoretical engineering of structural, electronic, and optical characteristics of double perovskite Sr_2XWO_6 (X=Co, Zn) for optical devices. J. Inorg. Organomet. Polym. (2024). https://doi.org/10.1007/s10904-024-03296-w
22. A. Dixit et al., A comprehensive DFT analysis of the physical, optoelectronic and thermoelectric attributes of Ba2lnNbO6 double perovskites for eco-friendly technologies. Mater. Sci. Eng.: B **307**, 117530 (2024)
23. S.K. Singh et al., Physical, optoelectronic and thermoelectric characteristics of double perovskite (Sr2ScBiO6) for green energy technology using Ab initio computations. RSC Adv. **13**, 35145–35160 (2023)
24. N. Erum et al., Vibrational and transport phenomenon in Cs2CdZnCl6 double perovskite: a DFT study. Solid State Ionics **403**, 116401 (2023)
25. K.K. Mishra, R. Sharma, A comparative study of the structural, electronic, and optical properties of Ca3SbCl3 halide perovskite using DFT-GGA and HSE06 functional for photovoltaic applications. Opt. Quant. Electron. **57**(1), 1–9 (2025)
26. K.K. Mishra, Exploring the physical, electrical and optical properties of Cs2LiInBr6 Perovskite: an extensive study utilizing DFT based GGA-PBE and HSE06 functionals. Braz. J. Phys. **55**(1), 1–4 (2025)
27. K.K. Mishra, Evaluating the potential of Ca3SbBr3 halide perovskite for photovoltaics: A structural, mechanical, and optoelectronic study using GGA-PBE and HSE06 functionals. Phys. Solid State. **66**(11), 464–475 (2024)
28. K.K. Mishra, Investigation of the double perovskite halides Cs2CuSbH6 (H=Cl, Br, I): electronic and optical properties for flexible electronics device applications. Phys. Solid State. **66**(10), 445–458 (2024)
29. K.K. Mishra, S. Chahar, R. Sharma, An extensive investigation of structural, electronic, and optical properties of inorganic perovskite Ca3AsCl3 for photovoltaic and optoelectronic applications: A first-principles approach using quantum ATK tool. Solid State Commun. **390**, 115623 (2024)
30. S. Chahar, K.K. Mishra, R. Sharma, Investigation of structural, electronic, and optical characteristics of a novel perovskite halide, Mg3AsCl3, for electronic applications. Phys. Status Solidi (b). **261**(10), 2400171 (2024)
31. K.K. Mishra, S. Chahar, R. Sharma, Machine learned analysis of Pnictides based Sr3PnCl3 (Pn=P, as, Sb) halide perovskites for next-generation solar applications. Phys. Lett. A **523**, 129817 (2024)
32. S. Chahar, C. Malan, K.K. Mishra, R. Sharma, Optimizing novel perovskite Mg3AsBr3 through uniaxial stress: a comprehensive study of its potential in solar and optoelectronic applications. Phys. Scr. **99**(9), 095994 (2024)
33. S. Chahar, K.K. Mishra, R. Sharma, Analysing the suitability of CaTiO3/Ca1–xSrxTiO3/SrTiO3 perovskite for fabrication of optoelectronic devices using QuantumATK tool: a study for electronic and optical properties. Phys. Scr. **99**(3), 035963 (2024)
34. B. Gurunani, D.C. Gupta, Tailoring the intrinsic magneto-electronic, mechanical, thermo-physical and thermoelectric response

of cobalt-based heusler alloys: an Ab initio insight. RSC Adv. **13**(43), 29959–29974 (2023)
35. B. Gurunani, D.C. Gupta, Exploring the electronic structure, mechanical behaviour, thermal and high-temperature thermoelectric response of CoZrSi and CoZrGe heusler alloys. Sci. Rep. **13**(1), 22834 (2023)
36. B. Gurunani, S. Ghosh, D.C. Gupta, Comprehensive investigation of half heusler alloy: unveiling structural, electronic, magnetic, mechanical, thermodynamic, and transport properties. Intermetallics. **170**, 108311 (2024)
37. B. Gurunani, D.C. Gupta, Exploring the multifaceted properties: structural, electronic, magnetic, mechanical, thermodynamic, transport, and optical characteristics of rhodium-based half-Heusler alloys. J. Mater. Sci. **59**(27), 12502–12525 (2024)
38. B. Gurunani, D.C. Gupta, Unravelling optoelectronic and transport properties in RuZrX (X = Si, Ge) alloys: insights from DFT. Adv. Theory Simulations. **8**(1), 2400621 (2025)
39. B. Gurunani, D.C. Gupta, A holistic approach to Understanding structural, magneto-electronic, thermoelectric, and thermodynamic properties of RhMnZ (Z = Si, Ge) half heusler alloys. Phys. Chem. Chem. Phys. **26**(48), 30002–30017 (2024)
40. B. Gurunani, D.C. Gupta, Half-metallicity and thermoelectric performance: A multifaceted investigation of Zr-based half-Heusler alloys. Mater. Sci. Engineering: B **311**, 117783 (2025)
41. B. Gurunani, D.C. Gupta, Unveiling half-metallic, thermoelectric and optoelectronic behavior of the new heusler alloy RbCrZ (Z = Si, Ge): a DFT perspective. Phys. Scr. **99**(11), 115542 (2024)
42. S.S. Essaoud, M.E. Ketfi, A.Y. Al-Reyahi, S.M. Al Azar, Computational prediction of Thermo-Elastic and charge carriers transport properties of Ba2MnReO6, Ba2NiReO6, and Sr2MnReO6 double perovskite compounds. Chem. Phys. Lett. **857**, 141694 (2024). Ketfi ME,
43. S.S. Essaoud, S.M. Al Azar, A.Y. Al-Reyahi, A.A. Mousa, N. Al-Aqtash, Mechanical, magneto-electronic and thermoelectric properties of Ba2MgReO6 and Ba2YMoO6 based cubic double perovskites: an Ab initio study. Phys. Scr. **99**(1), 015908 (2023)
44. B. Rameshe et al., Electronic structure, structural phase stability, optical andthermoelectric properties of Sr2AlM'O6 (M'= Nb and Ta) from first principle calculations. Comput. Condens. Matter **4**, 13–22 (2015)
45. S. Haid et al., Thermoelectric, structural, optoelectronic and magnetic properties of double perovskite Sr2CrTaO6: first principle study. Mater. Sci. Engineering: B **245**, 68–74 (2019)
46. K.A. Parrey, S. Rubab et al., Electronic structure, optical and transport properties of double perovskite La2NbMnO6: a theoretical Understanding from DFT calculations. J. Electron. Mater. **47**, 3615–3621 (2018)
47. S.A. Dar et al., Investigation on the electronic structure, optical, elastic,mechanical, thermodynamic and thermoelectric properties of wide band gap semiconductor double perovskite Ba2InTaO6. RSC Adv. **9**, 9522–9532 (2019)
48. S.A. Khandy et al., Forecasting electronic-band structure and magnetism in complex double perovskite Ba2CdReO6, AIP Conference Proceedings, AIP Publishing LLC, 2020, p. 030359
49. S. Al-Qaisi et al., First- principles investigations of Ba2NaIO6 double perovskite semiconductor: material for low-cost energy technologies. Mater. Chem. Phys. **275**, 125237 (2022)
50. A. Aziz et al., Theoretical investigation of X2NaIO6 (X = Pb, Sr) double perovskites for thermoelectric and optoelectronic applications. Phys. B: Condens. Matter **630**, 413694 (2022)
51. A. Hanif et al., Theoretical investigation of physical properties ofSr2XNbO6 (X = La, Lu) double perovskite oxides for optoelectronic and thermoelectric applications, Int. J. Energy Res. (2022)
52. R.K.V. Pillai, Development and characterization of visible light driven Ba2YBiO6 photocatalyst forthe degradation of organic compounds, AIP Conference Proceedings, AIP Publishing LLC, 2021, p. 030002
53. K. Schwarz et al., Electronic structure calculations of solids using the WIEN2k package formaterial sciences. Comput. Phys. Commun. **147**, 71–76 (2002)
54. P. Blaha et al., WIEN2K, An augmented plane wave + local orbitals program for calculating crystal properties, K. Schwarz (ed.), Vienna University of Technology, Austria, (2001)
55. J.P. Perdew et al., Generalized gradient approximation made simple. Phys. Rev. Lett. **77**, 3865 (1996)
56. F. Tran et al., Accurate band gaps of semiconductors and insulators with a semilocal exchange-correlation potential. Phys. Rev. Lett. **102**, 226401 (2009)
57. F.M. Moucherek, W.O. Santos, A.L. Novais, E. Moreira, D.L. Azevedo, Prediction of electronic and optical properties of monoclinic 1T'-phase OsSe2 monolayer using DFT principles. Mater. Today Commun. **33**, 104764 (2022)
58. W.O. Santos, A.M. Rodrigues, de E.R. Novais, N.F. Frazão, A.D. Novais, do D. Nascimento Souza, DFT and DFPT calculations of the structural, electronic, optical, vibrational and thermodynamic properties of silicon tetraborate. Comput. Condens. Matter. **35**, e00796 (2023)
59. W.O. Santos, F.M. Moucherek, A.C. Dias, E. Moreira, D.L. Azevedo, 1T'-RuO 2 monolayer: First-principles study of excitonic, optoelectronic, vibrational, and thermodynamic properties. J. Mater. Res. **38**(15), 3677–3689 (2023)
60. W.O. Santos, F.M. Moucherek, A.C. Dias, E. Moreira, D.L. Azevedo, Structural, optoelectronic, excitonic, vibrational, and thermodynamic properties of 1T'-OsO2 monolayer via ab initio calculations. J. Appl. Phys. (2023). https://doi.org/10.1063/5.0156245
61. W.O. Santos, L.S. Barbosa, E. Moreira, D.L. Azevedo, First-Principles investigation of the OsI 2 monolayer: A novel Two-Dimensional dihalide material for optoelectronic applications. Braz. J. Phys. **55**(1), 11 (2025)
62. W. Kohn, L.J. Sham, Self-consistent equations including exchange and correlation effects. Phys. Rev. **140**(4A), A1133 (1965)
63. A. Nazir et al., A density functional theory study of the structural, mechanical, optoelectronics and thermoelectric properties of InGeX3 (X = F, Cl) perovskites. Polyhedron. **257**, 117009 (2024)
64. C. Ambrosch-Draxl et al., Linear optical properties of solids within the full-potential linearized augmented Planewave method. Comput. Phys. Commun. **175**(1), 1–14 (2006)
65. G. Kresse, J. Furthmüller, Efficient iterative schemes for Ab initio total-energy calculations using a plane-wave basis set. Phys. Rev. B **54**, 11169–11186 (1996)
66. Q. Dai, Q.Q. Liang, T.Y. Tang, H.X. Gao, S.Q. Wu, Y.L. Tang, Insights on structural, elastic, electronic, optical and thermodynamic properties and population analysis of double perovskite oxide Ba2MgXO6 (X = Se, Te). Mater. Sci. Semiconduct. Process. **171**, 108003 (2024)
67. S. Saad Essaoud, M.E. Ketfi, S. Al Azar, A.Y. Al-Reyahi, A. Mufleh, Computational study of structural parameters, magnetic properties, half metallicity, and linear optical characteristics of transition-metal oxide double perovskites: Ba2MnReO6, Ba2NiReO6, and Sr2MnReO6. Indian J. Phys. **25**, 1–8 (2024)
68. S.S. Essaoud, M. Radjai, A. Bouhemadou, M.E. Ketfi, D. Allali, Fundamental physical features of the rhombohedral structure of double perovskite compounds Ba2NbBO6 (B = As, Sb, and Bi). Chem. Phys. **591**, 112578 (2025)
69. A.M. Tighezza et al., A DFT approach to study the vacancy ordered lead free double inorganic Perovskites Na2PtX6 (X = Cl, Br) for sustainable technologies. J. Inorg. Organomet. Polym. Mater. **35**, 1–18 (2024)

70. M. Manzoor et al., Exploring the structural, electronic, optical, and thermoelectric properties of potassium-based double perovskites K2AgXI6 (X=Sb, Bi) compounds: A DFT study. Mater. Sci. Engineering: B **287**, 116122 (2023)
71. M.Z. Kazim et al., Lead-free Cs2InAsX6 (X=Cl, Br) halide double perovskites: A DFT perspective on their potential for sustainable energy applications. J. Phys. Chem. Solids. **189**, 111954 (2024)
72. G.K. Madsen et al., BoltzTraP. A code for calculating band-structure dependent quantities. Comput. Phys. Commun. **175**(1), 67–71 (2006)
73. G.A. Slack, The thermal conductivity of nonmetallic crystals. Solid State Phys. **34**, 1–71 (1979)
74. J.A. Abraham et al., Computational prediction on the stability, Opto-electronic and thermoelectric properties of double perovskite compound Sr_2CrBiO_6: a first principles investigation. J. Inorg. Organomet. Polym. (2024). https://doi.org/10.1007/s10904-024-03500-x
75. M. Manzoor et al., Probing the optoelectronic and thermoelectric performance of inorganic halide perovskite Rb_2KInI_6 for renewable energy applications via DFT computations. J. Inorg. Organomet. Polym. (2024). https://doi.org/10.1007/s10904-024-03456-y
76. A. Kumari et al., Tuning optoelectronic and thermoelectric attributes of Na2GeX6 (X = Br, Cl) halide double perovskites for high-efficiency solar cells applications. Mater. Sci. Eng. **298**, 116875 (2023)
77. M. Jamil et al., Screening the structural, tuning band gaps, optical and thermal properties of inorganic A_2AgRhF_6 (A=Na, Rb) double perovskites halide using DFT calculations. J. Inorg. Organomet. Polym. (2024). https://doi.org/10.1007/s10904-024-03419-3
78. M. Aslam et al., Effect of anion on optoelectronic and thermoelectric properties cubic double perovskites A_2(Sr, Ba)$WMgO_6$ for Low-Cost energy technologies: A computational simulation study. J. Inorg. Organomet. Polym. (2024). https://doi.org/10.1007/s10904-024-03376-x
79. A. Otero-de-la-Roza et al., Gibbs2: a new version of the quasi-harmonic model code. II. Models for solid-state thermodynamics, features and implementation. Comput. Phys. Commun. **182**, 2232–2248 (2011)
80. M. Rudra et al., Phase transitions in oxygen-intercalated pseudocapacitor Pr_2MgMnO_6 electrode: A combined structural and conductivity analysis. Mater. Sci. Engineering: B **307**, 117517 (2024)
81. A. Shareef et al., Third order nonlinear optical properties and electrochemical performance of La_2CoMnO_6 double perovskite. Mater. Sci. Engineering: B **289**, 116262 (2023)
82. A. Besbes et al., The first principle calculations of magnetic and thermoelectric properties of Ba_2CeCoO_6 with GGA and mBJ approximations. Comput. Condens. Matter. **19**, e00380 (2019)
83. R. Das et al., Structural and electrical characteristics of double Perovskite: Sr_2FeMoO_6. Mater. Sci. Engineering: B **281**, 115715 (2022)
84. P. Mondal et al., First-principles calculations to investigate effect of uniaxial stress on optical and magnetic properties of Sr_2XWO_6 (X = Fe, Co & Ni). Mater. Sci. Eng.: B **298**, 116875 (2023)
85. A. Jamal et al., IRelast package. J. Alloys Compd. **735**, 569–579 (2018)
86. R. Ji et al., Influence of dielectric and machining parameters on the process performance for electric discharge milling of SiC ceramic. Int. J. Adv. Manuf. Technol. **59**(1), 127–136 (2012)
87. C. Shi et al., Atomic imaging and optical properties of InAs/In0.5Ga0.5As0.5Sb0.5 type II superlattice. Appl. Phys. Lett. **124**(25), 251101 (2024)
88. J. Wang et al., Simulation of residual stress and distortion evolution in dual-robot collaborative wire-arc additive manufactured Al-Cu alloys. Virtual Phys. Prototyp. **19**(1), e2409390 (2024)
89. M. Huang et al., Optimizing crack initiation energy in austenitic steel via controlled martensitic transformation. J. Mater. Sci. Technol. **198**, 231–242 (2024)
90. W. Yu et al., Discovering novel γ-γ′ Pt-Al superalloys via lattice stability in Pt3Al induced by local atomic environment distortion. Acta Materialia **281**, 120413 (2024)
91. T. Fan et al., Nucleation and growth of L12-Al3RE particles in aluminum alloys: A first-principles study. J. Rare Earths. **41**(7), 1116–1126 (2023)
92. W. Luo et al., Effect of volumetric energy density on the mechanical properties and corrosion resistance of laser-additive-manufactured AlCoCrFeNi2.1 high-entropy alloys. J. Alloys Comp. **1010**, 178032 (2025)